AIAA Propulsion and Energy Forum
August 24-28, 2020, VIRTUAL EVENT
AIAA Propulsion and Energy 2020 Forum

10.2514/6.2020-3775

Distortion Elimination for Serpentine Inlet Using CoFlow Jet Flow Control with Variation of Mach Numbers

Kewei Xu *, Gecheng Zha †
Dept. of Mechanical and Aerospace Engineering
University of Miami, Coral Gables, Florida 33124
E-mail: gzha@miami.edu

Abstract

This paper numerically investigates Coflow Jet (CFJ) active flow control (AFC) for eliminating M2129 serpentine inlet distortion with throat Mach number (M_{th}) varying from 0.42 to 0.79. The 3D Reynolds Averaged Navier-Stokes (RANS) simulation is conducted with one-equation Spalart-Allmaras (S-A) turbulence model. The CFD simulation is validated with the experiment of AGARD test cases. The predicted total pressure recovery is in good agreement with experiment with the maximum discrepancy less than 1%. The distortion coefficient (DC_{60}) is also in a reasonable agreement with the experiment. The simulation also agrees very well with the experiment for the wall static pressure distribution. For the CFJ S-duct, the horn shaped slot geometry is adopted for the CFJ injection and suction slots to minimize the flow separation caused by CFJ. For all the throat Mach numbers, the engine face distortion coefficient is reduced to less than 1%, virtually eliminated by CFJ. Besides, the total pressure recovery is also significantly enhanced, especially at the high throat Mach number of 0.79. The study also indicates that a higher throat Mach number requires a lower CFJ power coefficient (P_C) to eliminate the flow separation and distortion. This numerical study suggests that it is possible to eliminate S-duct distortion by using CFJ active flow control.

Nomenclature

AFC	Active flow control
AIP	Aerodynamic Interface Plane
CFJ	Co-flow jet
C_μ	Jet momentum coefficient
DC_{60}	Distortion factor of 60 degree, $DC_{60} = \frac{Pt_{AIP} - Pt_d}{q_{AIP}}$
M	Mach number
M_{th}	Throat Mach number
P	Power consumption of CFJ actuator
P_c	Power coefficient
Pt_{AIP}	Averaged total pressure at AIP
Pt_d	Averaged total pressure at distortion section
q_{AIP}	Dynamic pressure at AIP

* Ph.D. candidate
† Professor, ASME Fellow, AIAA associate Fellow

Re	Reynolds number
R_i	Duct inlet radius
$ZNMF$	Zero-net mass flux
c	Subscript, stands for corrected
j	Subscript, stands for jet
β	Circumferential slot angle
γ	Air specific heats ratio
δ	Total pressure recovery
Γ	Pressure ratio
η	Micro-comprssor efficiency
θ	Duct circumferential angle

1 Introduction

Serpentine ducts (S-ducts) are widely studied in recent decades. Combined with boundary layer ingestion, a short S-duct is able to significantly reduce the fuel consumption and ram drag [1, 2]. For military aircraft, S-ducts also reduce radar cross-sectional visibility due to the buried engines [3, 4]. However, a major challenge of S-ducts is flow separation, which is induced by the high curvature wall at duct bend. The consequences can be severe, such as triggering flow distortion, reducing compressor stall margin, and exciting fan blade vibration.

To mitigate flow separation inside S-ducts, a passive flow control method using vortex generator is studied numerically and experimentally [5, 6, 7, 8]. Based on the CFD simulated vortex generators, the engine face distortion of M2129 S-duct is reduced by up to 80% [9]. Jirasek et al [10] conduct an optimization study of vortex generators flow control and find the effectiveness mainly depends on their heights and their locations in the flow separation.

For active flow control methods, fluidic-oscillating jets [11, 12] are used on a serpentine offset diffuser to generate streamwise vorticity and reduce total pressure distortion. It is able to reduce the aerodynamic interface plane (AIP) distortion by more than 60%. Harrison et al [13, 14] propose an ejector-pump concept to employ injection and suction simultaneously. It reduces the demand for bleed air from the compressor. With the ejector-pump model, the maximum reduction of engine-face distortion of 75% is achieved. Rudin et al [15] apply steady suction and blowing on the S-duct of a Blended Wing-Body (BWB) and achieve an improvement of 4.3% in total pressure recovery and 70% in DC_{60} reduction.

The Coflow Jet (CFJ) [16, 17, 18, 19, 20, 21, 22, 23, 24, 25, 26] is a zero-net-mass-flux flow control that draws flow from a suction slot at downstream and ejects the flow at upstream using micro-compressor actuators. Recently, Xu et al [27, 28, 29, 30] apply CFJ on the NASA hump and some aircraft control surfaces, which demonstrate its high effectiveness and energy efficiency in separation removal. Xu and Zha [31] apply CFJ AFC to mitigate M2129 inlet distortion at Mach number of 0.79. With a configuration using a horn shape injection and suction slot on the lower duct surface, the distortion coefficient DC_{60} is reduced by 96%. However, the study [31] is only for a single throat Mach number. The purpose of this paper is to further refine the CFJ flow control configuration and study the distortion behavior across a range of Mach numbers, which are required to cover the whole aircraft flight envelop.

2 The Coflow Jet Parameters

To facilitate the description of CFJ control surface performance, several important parameters are given below.

2.1 Jet Momentum Coefficient

The injection jet momentum coefficient C_μ is used to describe the CFJ strength as:

$$C_\mu = \frac{\dot{m} V_j}{\frac{1}{2}\rho_\infty {V_\infty}^2 A_{ref}} \tag{1}$$

where $\dot{m}$ is the injection mass flow, V_j is the mass-averaged injection velocity, ρ_∞ and V_∞ denote the reference density and velocity at inlet, and A_{ref} is the reference area defined as S-duct inlet area.

2.2 Power Coefficient

The CFJ power required is determined by the total enthalpy rise from the suction slot outlet to the injection slot inlet [17]. The total enthalpy rise can be achieved by the embedded micro-compressors. The power required by the CFJ can be expressed as:

$$P = \frac{\dot{m} H_{t2}}{\eta}(\Gamma^{\frac{\gamma-1}{\gamma}} - 1) \tag{2}$$

where, $\dot{m}$ is the CFJ mass flow rate, H_{t2} is the total enthalpy at the suction slot, Γ is the total pressure ratio between the injection and suction, and η is the pumping system efficiency.

Eq. (3) indicates that the power required by the CFJ is linearly determined by the mass flow rate and exponentially by the total pressure ratio. This relationship in fact applies to all active flow controls based on fluidic actuators. Thus, C_μ can not be used to represent the power consumption of active flow control [17, 32]. For example, a high C_μ could have a substantially lower power consumption than a smaller C_μ if the large C_μ is created by a high mass flow rate and low jet velocity, which only needs a significantly lower total pressure ratio [32, 33].

$$P_c = \frac{P}{\frac{1}{2}\rho_\infty V_\infty^3 A_{ref}} \tag{3}$$

where P is the CFJ required power defined in Eq. (2).

3 The Numerical Algorithm

The in-house high order accuracy CFD code Flow-Acoustics-Structure Interaction Package (FASIP) is used to conduct the numerical simulation. The 3D Reynolds Averaged Navier-Stokes (RANS) equations with one-equation Spalart-Allmaras [34] turbulence model is used. A 3rd order WENO scheme for the inviscid flux [35, 36, 37] and a 2nd order central differencing for the viscous terms are employed to discretize the Navier-Stokes equations. The low diffusion E-CUSP scheme used as the approximate Riemann solver suggested by Zha et al [38] is utilized with the WENO scheme to evaluate the inviscid fluxes. Implicit time marching method using Gauss-Seidel line

relaxation is used to achieve a fast convergence rate [39]. Parallel computing is implemented to save wall clock simulation time [40]. The FASIP code is intensively validated for CFJ airfoil simulations [17, 18, 19, 20, 23, 24, 25, 27, 28, 29, 30, 31, 41, 42, 43].

4 Baseline Serpentine Duct Validation

The baseline serpentine duct (S-duct) studied in the present research with the side-view shown in Fig. 1 is adopted from [44]. The throat is located at the origin point of the axial axis. The duct is tested experimentally in the AGARD study [45]. The S-duct is approximately 2 ft in length and the throat is 0.4225 ft in diameter, which is located at the end of the upstream constant-area section. The outlet diameter is 0.5 ft with a diverging area ratio of outlet to inlet of 1.4. The engine face, or the aerodynamic interface plane (AIP), is located at 1.6 ft downstream of the duct throat. The duct inlet conditions for the simulation are adopted from the AGARD test cases, which have the total pressure of 101,216 Pa, total temperature of 293 K and Re of 2.36 million based on the inlet diameter. The inlet velocity is imposed to be normal to the inlet surface.

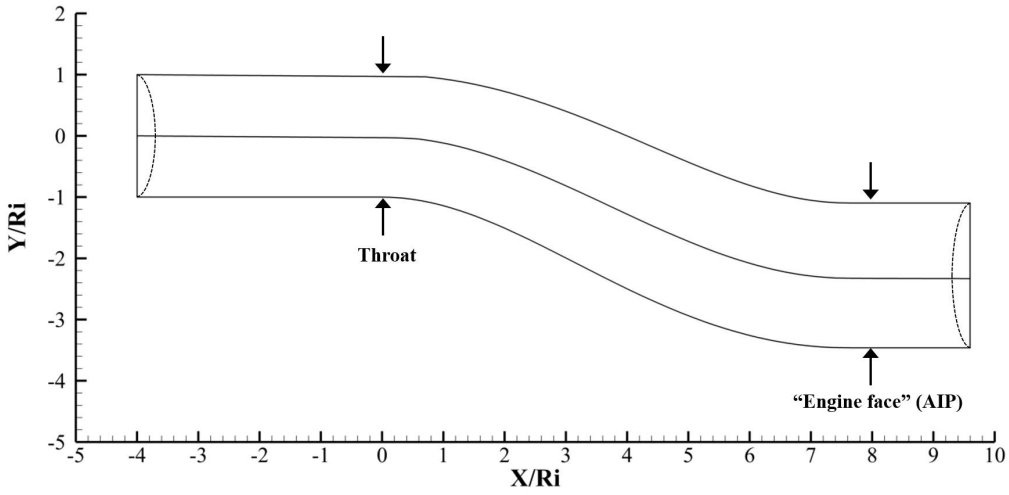

Figure 1: Side-view of the baseline S-duct

The mesh topology is shown in Fig. 2. Only half of the S-duct is simulated due to the symmetric geometry. The S-duct bend section is refined and a butterfly grid treatment is used for the duct cross-section meshing as shown in Fig. 2 (left). The overall mesh size is 2.0 million points, equivalent to 105 $\times$ 281 $\times$ 68 points in the streamwise, circumferential and radial direction. The boundary condition at the S-duct inlet has the specified total pressure, total temperature and flow angle. The outlet boundary condition uses a specified static pressure. Non-slip wall boundary condition is enforced on the duct wall and symmetry boundary condition is applied on the S-duct symmetric plane. The center-body of the S-duct at the downstream of the AIP is not simulated.

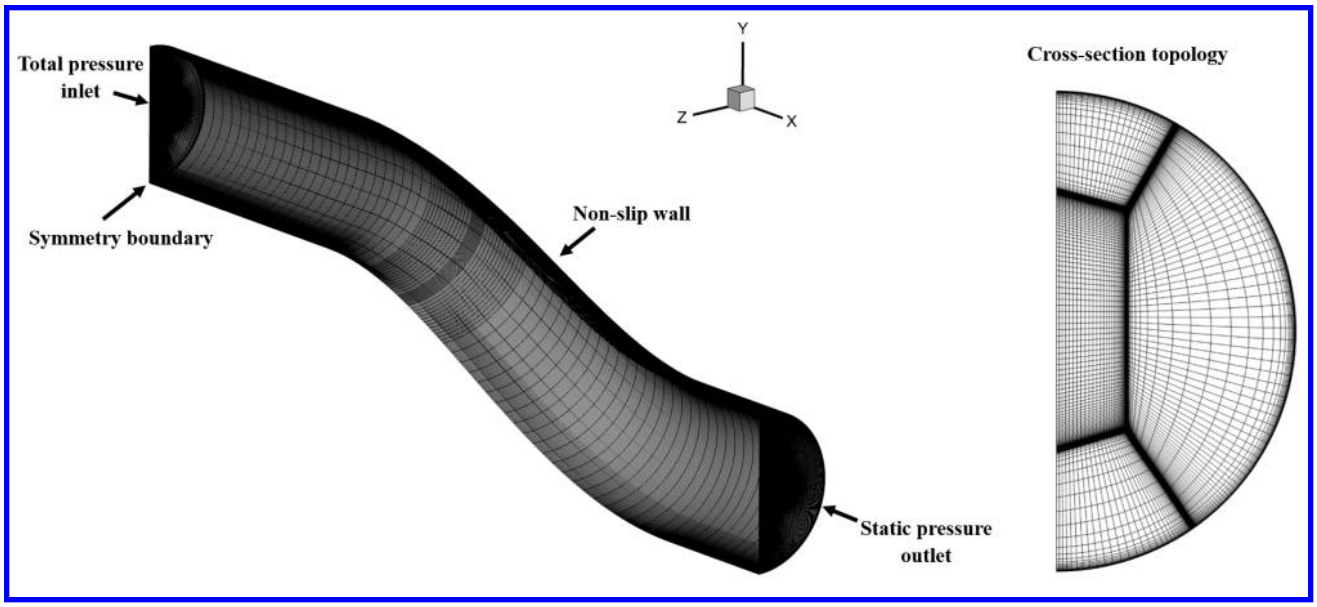

Figure 2: Mesh topology of the baseline S-duct

The plot on the left of Fig. 3 shows the computed total pressure recovery δ (right) at AIP and Mach contours of the baseline S-duct on the symmetric plane (left) at the throat Mach number (M_{th}) of 0.79. The total pressure recovery is calculated by the total pressure at AIP divided by the total pressure at the S-duct inlet, which is constant and uniform on the inlet. Massive flow separation occurs at the duct bend section, which causes significant total pressure loss and distortion at the bottom of AIP. With the throat Mach number of 0.79, the predicted total pressure recovery is 95.9%, which has a less than 1% discrepancy from the experimental value of 95.7%. The predicted distortion coefficient DC_{60} at AIP is 40.7% and has a deviation from the measured value of 40.4% by less than 1%. The DC_{60} [46] is the distortion coefficient computed based on a sector of 60° as shown in Fig. 3. The distortion sector with a 60° is usually considered as a required range [46]. The formulation of DC_{60} is the following,

$$DC_{60} = \frac{Pt_{AIP} - Pt_d}{q_{AIP}} \tag{4}$$

Where the Pt_{AIP} is area-averaged total pressure at AIP, Pt_d is area-averaged total pressure in the worst 60 degree sector of the engine face, and q_{AIP} is averaged dynamic pressure at AIP. Since the Pt_d is in the distortion area suffering more loss, the value should be lower than the Pt_{AIP}. Note that the values used for DC_{60} calculation follows the same data reduction routine used in the experiment [45, 47], where Pt_{AIP} and Pt_d are calculated based on the 72-probe measured total pressure. Dynamic pressure q_{AIP} is calculated by assuming incompressible flow at AIP, where the velocity uses the value at AIP.

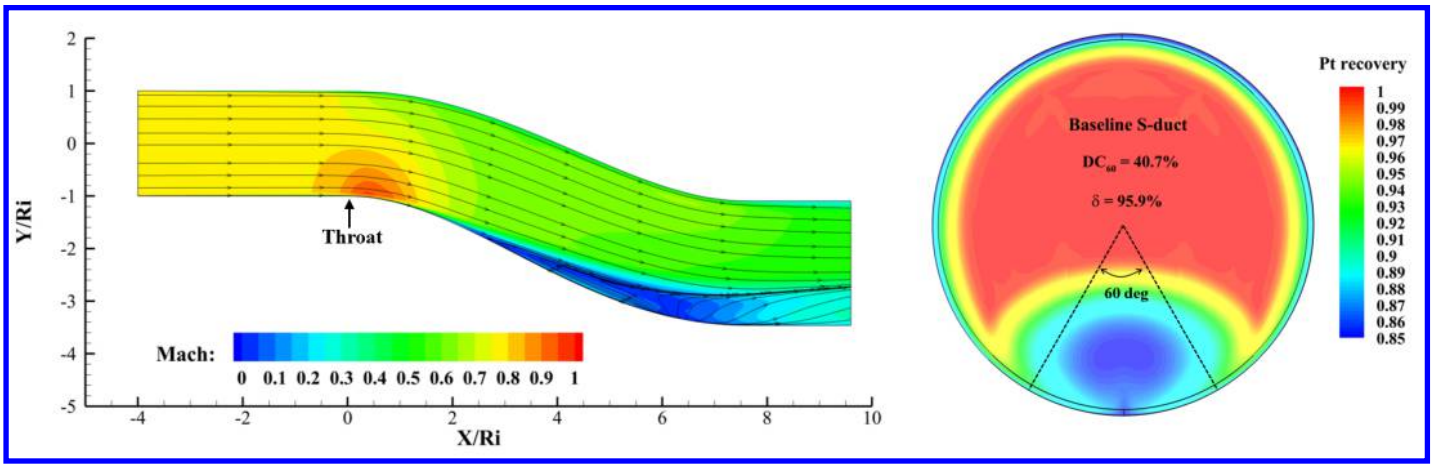

Figure 3: Computed Mach contours of the baseline S-duct and total pressure recovery at AIP

Fig. 4 compares the computation with the experiment for the total pressure recovery and distortion coefficient (DC_{60}) at various throat Mach numbers. The CFD results predicted by Wind-US code [48] is also presented for comparison. A good agreement is achieved between the predicted total pressure recovery and the experiment. A larger discrepancy is observed for the DC_{60} prediction, which may be caused by the absence of center-body downstream of the AIP. However, the trend agrees with the experiment very well. The present CFD prediction agrees with the experiment better than the Wind-US [48] at the high Mach number range. For the low Mach number of 0.42, the two CFD predictions are similar.

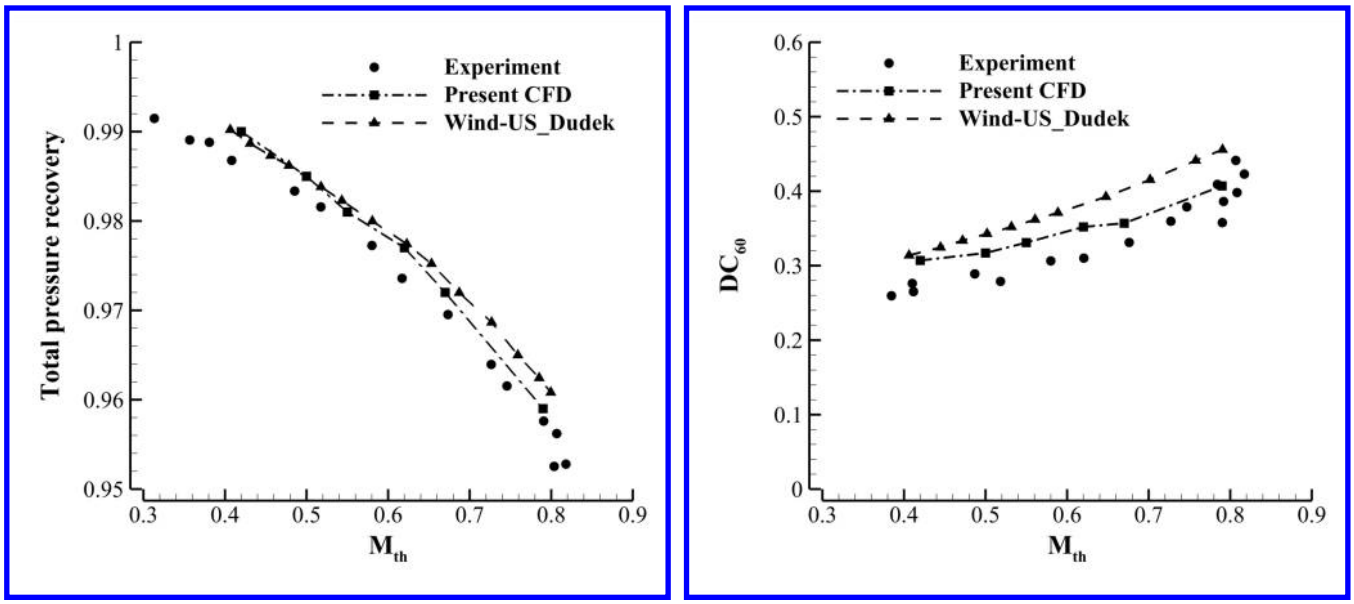

(a) Total pressure recovery (b) Distortion coefficient

Figure 4: The baseline S-duct performance with various throat Mach numbers

Fig. 5 shows the wall static pressure distribution along the axial direction, where θ of 0° and 180° are the circumferential angles representing the top surface and bottom surface of the duct. The pressure distributions are presented with two duct throat Mach numbers, 0.42 and 0.79. A good agreement is achieved between the predicted results and the experiment with the maximum discrepancy of 4.8%. The deviation is more at the bottom surface,

which has the flow separation due to S-duct bend.

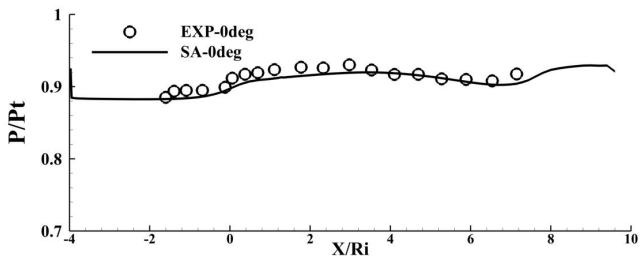

(a) 0 deg surface, M_{th}=0.42

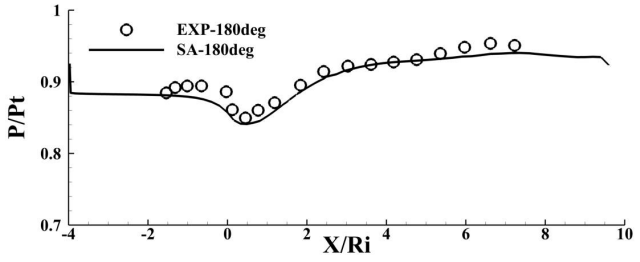

(b) 180 deg surface,M_{th}=0.42

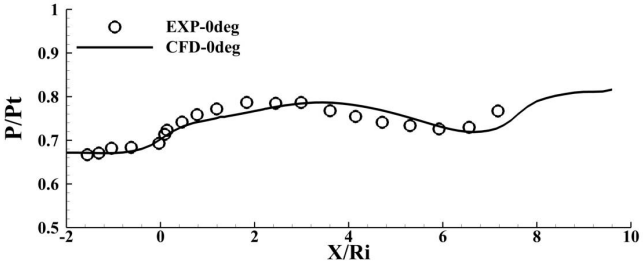

(c) 0 deg surface, M_{th}=0.79

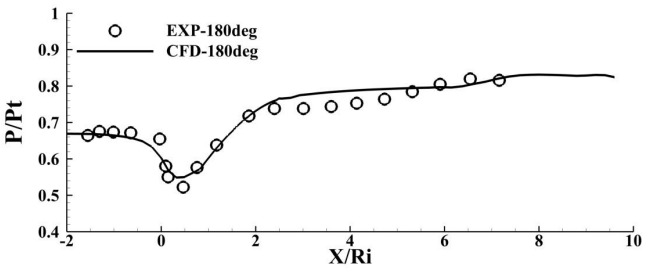

(d) 180 deg surface,M_{th}=0.79

Figure 5: Wall static pressure distributions

5 CFJ Serpentine Duct

The CFJ S-duct configuration is shown in Fig. 6 to illustrate how the CFJ is incorporated with the S-duct. The CFJ S-duct is created by placing an injection slot (in blue) at the start of the duct turning immediately downstream of the throat and placing a suction slot (in orange) at the duct bend. Detailed geometrical parameters are shown in Table 1. The present geometry is optimized based on the previous parametric studies [31]. The injection jet enters the duct tangentially to the local wall surface. The same amount of mass flow is withdrawn smoothly into the suction duct. To make the injection and suction smooth, the bottom wall surface is translated radially outward by a concentric circle with the radius increased by 0.5% of the inlet radius. The CFJ will energize the boundary layer to sustain the adverse pressure gradient of the duct diffusion and make the flow attached. The circumferential horn shaped slot geometry (shown in gray) is adopted for the CFJ injection and suction slots to minimize the separation caused by the CFJ duct wall on the two ending sides. A circumferential width of the slot of CFJ ducts is expressed by its circumferential angle (β) in Fig. 6. In this study, the injection and suction β angles are 100° and 110° respectively. This is an improved design from the previous configuration in [31] by increasing the suction slot width from 90° to 110°, which is beneficial to eliminate the distortion at the AIP with broader suction of the boundary layer.

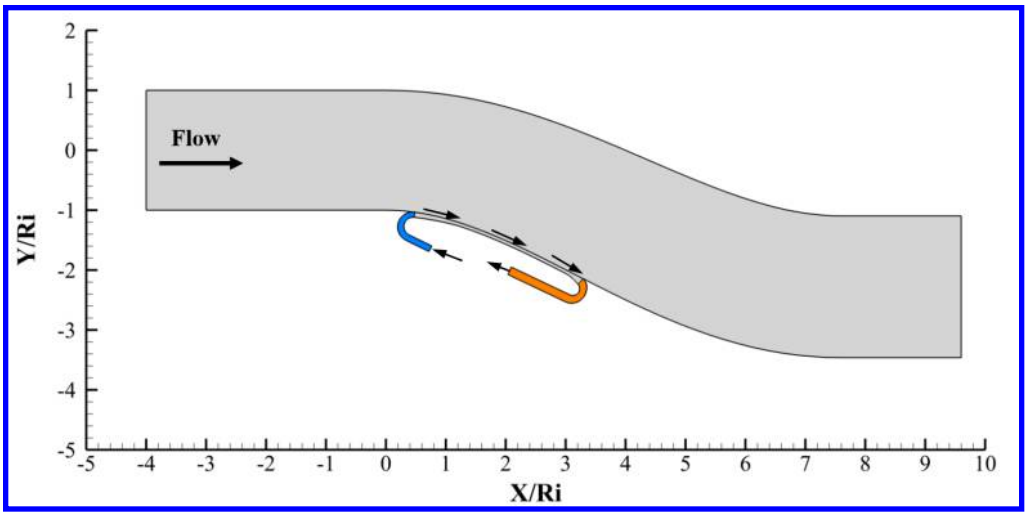

(a) CFJ S-duct at symmetric plane view

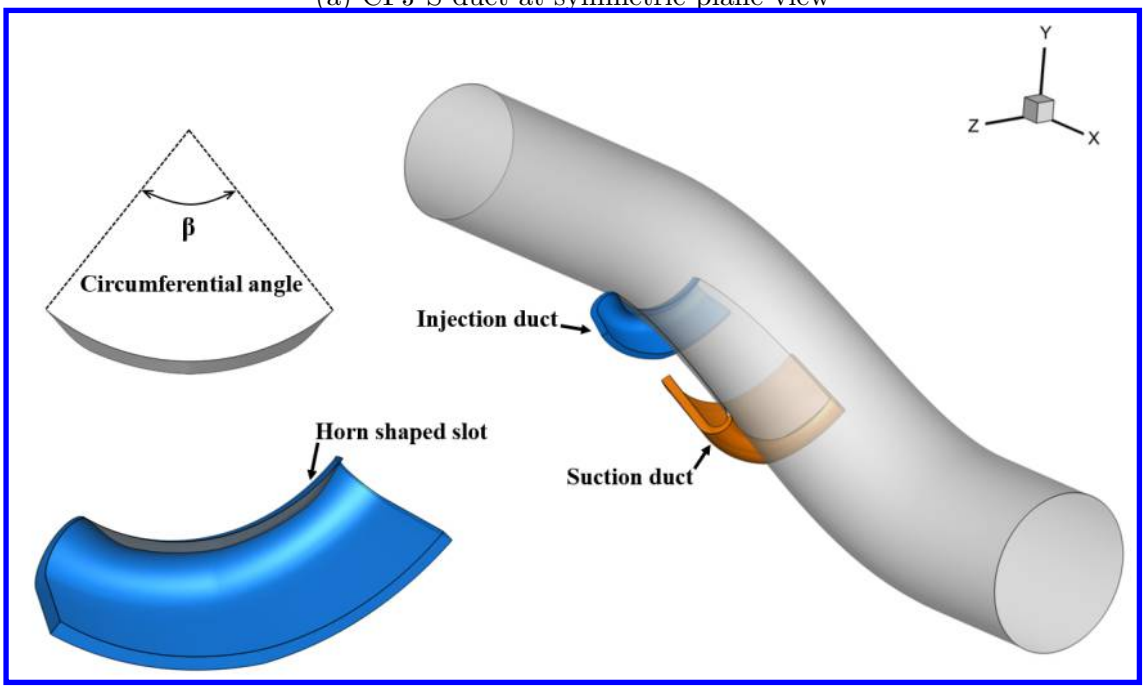

(b) 3D geometry of CFJ S-duct

Figure 6: Illustration of CFJ S-duct

Table 1: Geometrical parameters of the CFJ S-duct

Inj Location (X/R_i)	Suc Location (X/R_i)	Inj β (°)	Suc β (°)
0.47	3.29	100	110

6 Performance of the CFJ S-duct

This section shows the results of the CFJ S-duct for four throat Mach numbers (M_{th}) of 0.42, 0.55, 0.68, 0.79. The goal is to reduce the AIP distortion coefficient (DC_{60}) to near 0 with minimized power coefficient (P_C). Since the DC_{60} of the baseline S-duct varies with M_{th}, the power coefficient required for distortion control is different among the cases. Fig. 7 shows the Mach number contours and streamlines at the symmetric plane for the CFJ S-duct at the four throat Mach numbers. The separation is removed for all the Mach numbers and the flow is well attached. A high energy jet is ejected through the injection slot and energizes the main flow to overcome the adverse pressure gradient at S-duct bend. The CFJ suction is fixed at 3.29 X/R_i, which is observed to be the optimum suction location in the previous study [31]. This is because 3.29 X/R_i is the geometry inflection location that the slope reaches the minimum and the local diffusion reaches the maximum. Placing the suction at such location most effectively energizes the flow boundary layer and prevents separation onset. This is consistent with the conclusions from the other study applying the CFJ to the NASA hump and a wind turbine airfoil [30, 49].

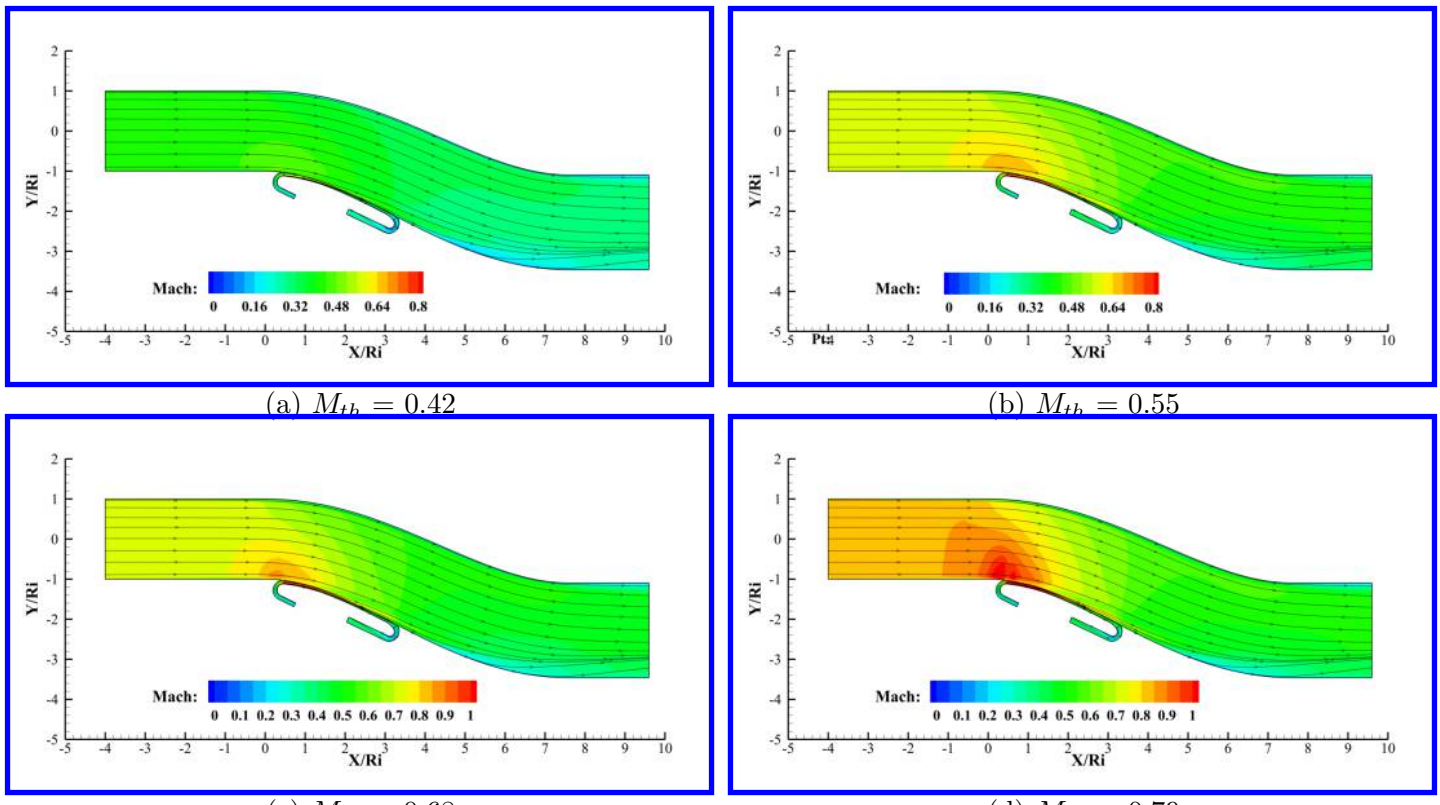

(a) $M_{th} = 0.42$ (b) $M_{th} = 0.55$

(c) $M_{th} = 0.68$ (d) $M_{th} = 0.79$

Figure 7: Mach contours of the CFJ S-duct at symmetry view

Fig. 8 shows the cross-sectional total pressure contours in the stream-wise direction. A high energy jet is injected through the CFJ injection duct and is gradually mixed with the S-duct main flow. The distortion is reduced via the mixing process between the high energy jet and the low total pressure main flow at duct bend.

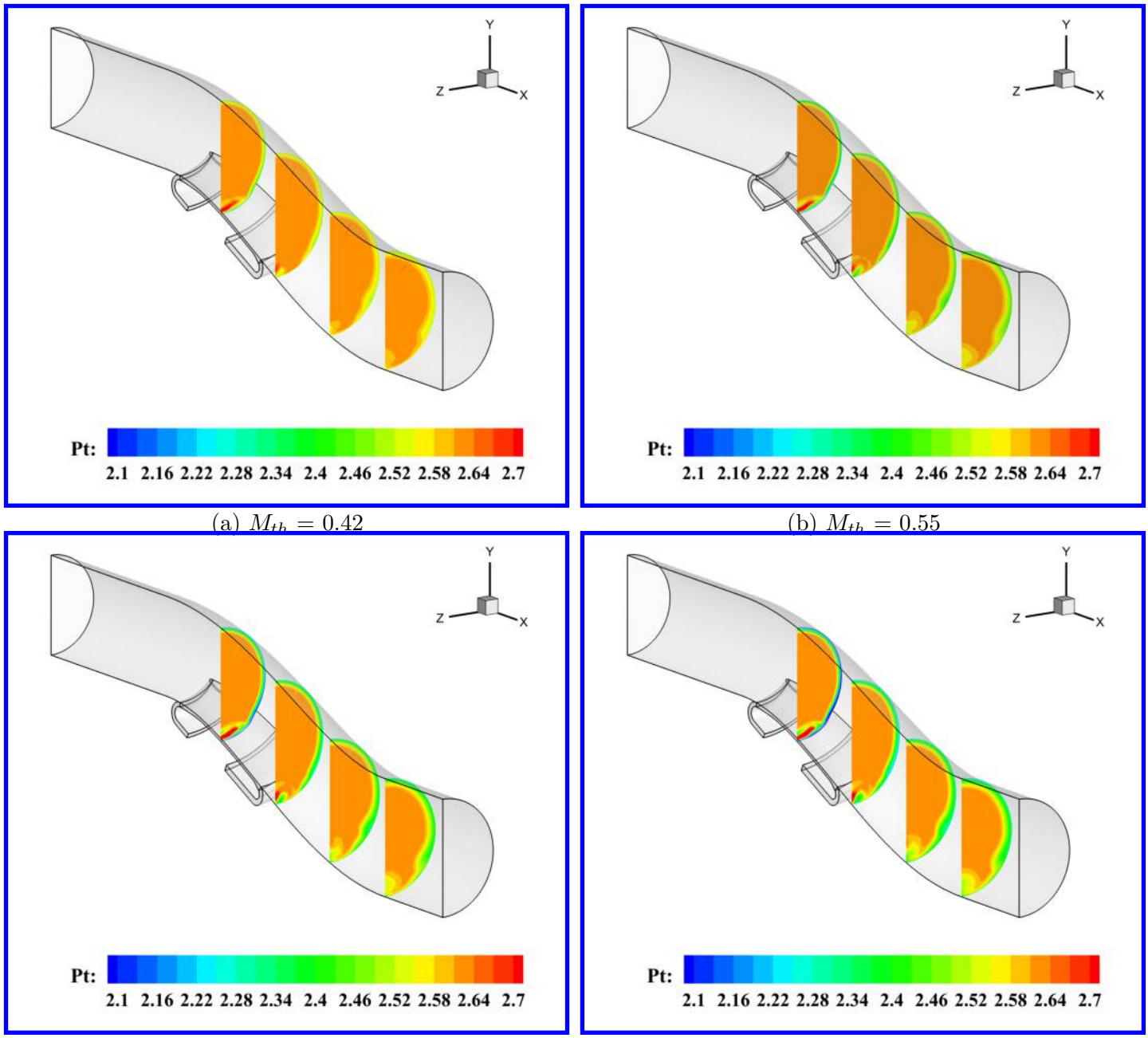

(a) $M_{th} = 0.42$ (b) $M_{th} = 0.55$

(c) $M_{th} = 0.68$ (d) $M_{th} = 0.79$

Figure 8: Total pressure contours along stream-wise of the CFJ S-duct

Fig. 9 shows the comparison of total pressure recovery contours between the baseline S-duct (left) and the CFJ S-duct (right) at the AIP. The DC_{60} is reduced to less than 1% in all the M_{th} cases and the total pressure at AIP is much more uniformly distributed than the baseline. Table 2 summarizes the performance of the CFJ S-duct in various M_{th}, where $\Delta\delta$ is the improvement of total pressure recovery in percentage, and ΔDC_{60} measures the reduction of distortion coefficient in percentage. The table indicates that a higher $\Delta\delta$ is achieved with a higher throat Mach number. This is because the flow separation and total pressure loss in the baseline S-duct are more severe with the increasing M_{th}. Since the CFJ reduces DC_{60} to the same level for all the M_{th} cases, the high M_{th} cases with more loss are recovered with higher total pressure. In terms of ΔDC_{60}, all cases have the similar

reduction of about 98%. As M_{th} is increased, the required momentum coefficient (C_μ) and power coefficient (P_C) for CFJ are decreased. However, the actual power is increased since the inlet velocity is increased with the throat Mach number. Table 2 also indicates that the CFJ required total pressure ratio is increased from 1.12 to 1.53 with the throat Mach number varying from 0.42 to 0.79. The CFJ injection Mach number is varied from 0.54 to 0.98.

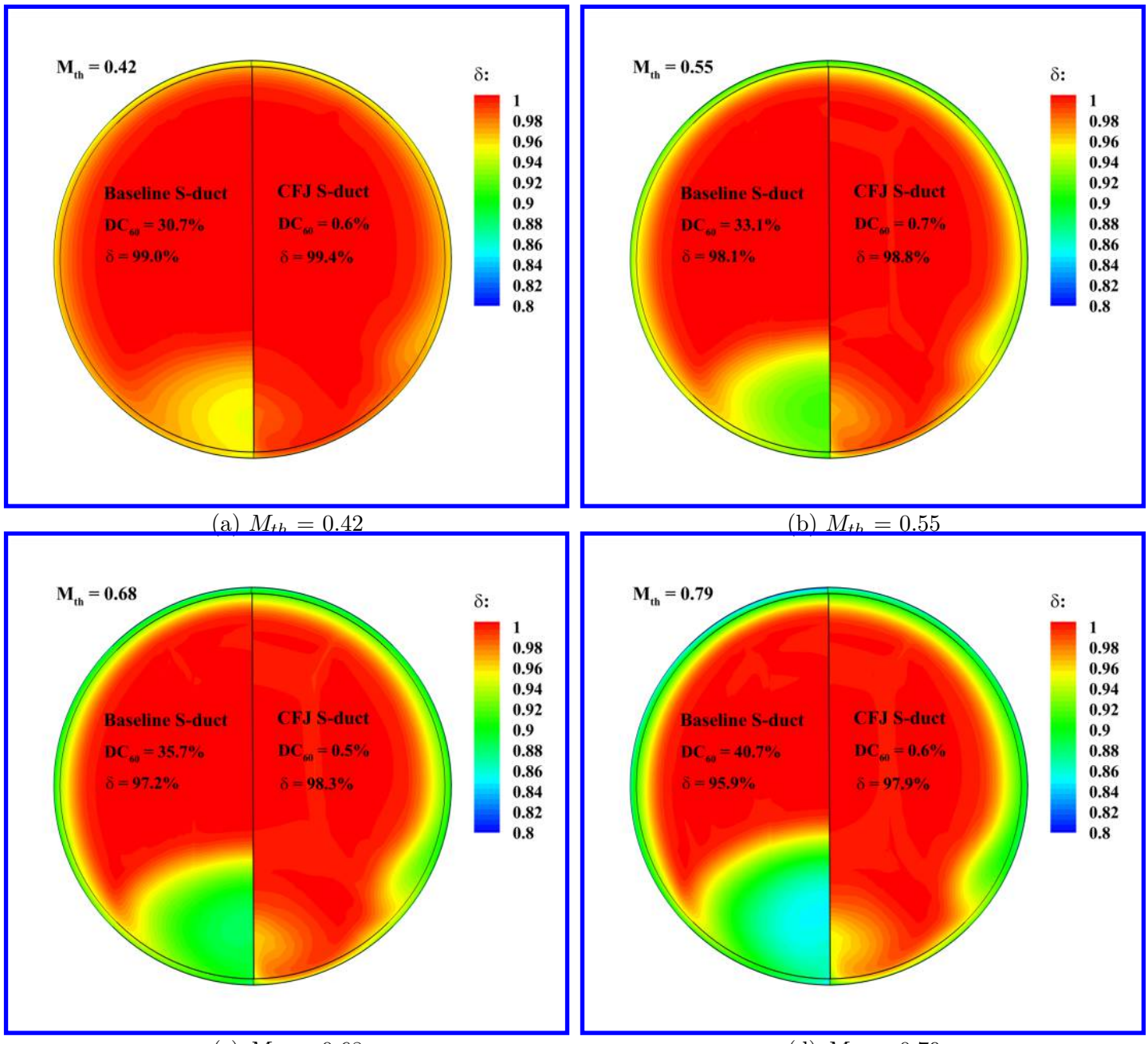

(a) $M_{th} = 0.42$ (b) $M_{th} = 0.55$

(c) $M_{th} = 0.68$ (d) $M_{th} = 0.79$

Figure 9: Total pressure recovery comparison at AIP between the CFJ and baseline S-ducts

Table 2: Performance of the baseline and CFJ S-ducts at AIP

M_{th}	Baseline		CFJ							
	δ	DC_{60}	C_μ	δ	$\Delta\delta$	DC_{60}	ΔDC_{60}	Γ	P_C	M_j
0.42	99.0%	30.7%	1.30	99.4%	0.4%	0.6%	-98.0%	1.12	0.52	0.54
0.55	98.1%	33.1%	1.29	98.8%	0.7%	0.7%	-97.9%	1.22	0.49	0.74
0.68	97.2%	35.7%	1.15	98.3%	1.1%	0.5%	-98.6%	1.38	0.48	0.93
0.79	95.9%	40.7%	0.94	97.9%	2.0%	0.6%	-98.5%	1.53	0.42	0.98

Fig. 10 compares the improvement of total pressure recovery δ and distortion coefficient DC_{60} between vortex generators (VGs) passive flow control [50] and CFJ active flow control. The advantages of the VGs are that they are simple to implement and do not require power input. However, the VGs achieve about DC_{60} of 5%, whereas the CFJ is able to drive the DC_{60} down to less than 1%, virtually removes the distortion. Furthermore, the CFJ achieves substantially higher total pressure recovery than that of the VGs. The total pressure recovery increment $\Delta\delta$ of the CFJ is about 1.5 times higher than that of the VGs at M_{th} of 0.79. This demonstrates the main advantage of the CFJ for its high effectiveness and high efficiency. The near zero distortion DC_{60} and largely enhanced total pressure recovery can significantly improve the downstream compressor efficiency and engine operation reliability.

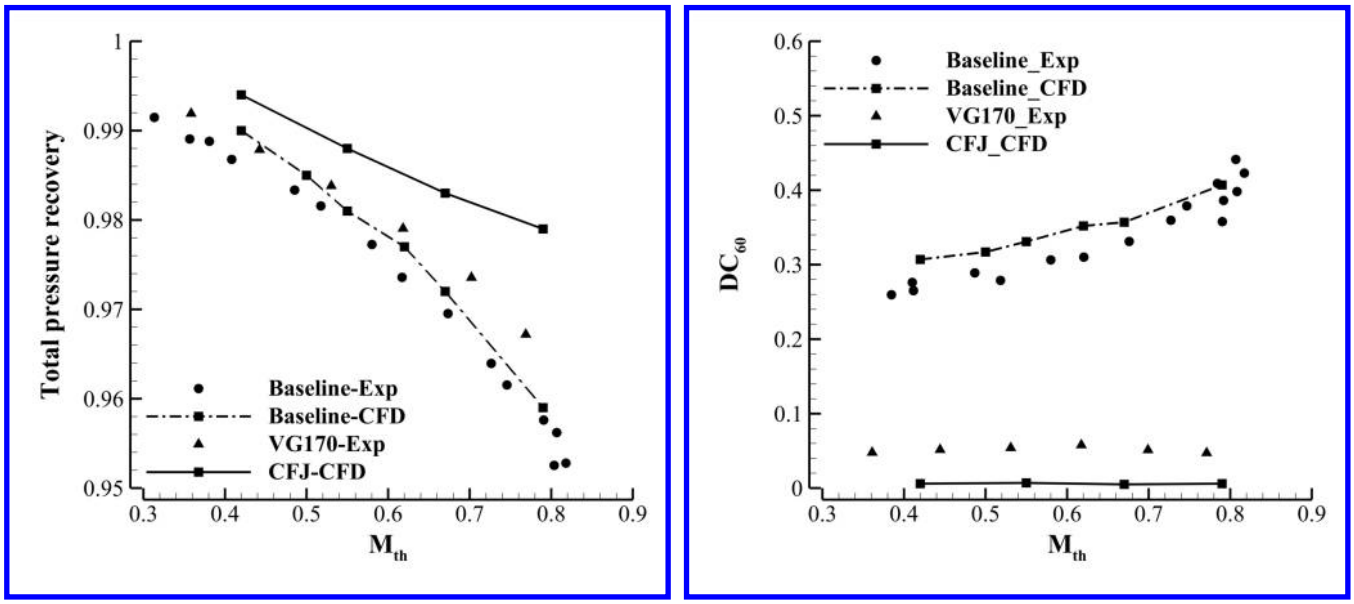

(a) Total pressure recovery (b) Distortion coefficient

Figure 10: Comparison of the baseline S-duct and controlled S-duct

7 Conclusions

This paper numerically investigates Coflow Jet (CFJ) active flow control (AFC) for eliminating M2129 serpentine inlet distortion with throat Mach number varying from 0.42 to 0.79. The CFD simulation is validated with the experiment of AGARD test cases. The predicted total pressure recovery is in good agreement with experiment with the maximum discrepancy less than 1%. The distortion coefficient (DC_{60}) is also in a reasonable agreement with

the experiment. The simulation also agrees very well with the experiment for the wall static pressure distribution. For the CFJ S-duct, the horn shaped slot geometry is adopted for the CFJ injection and suction slots to minimize the flow separation caused by CFJ at the end of the slot. The injection and suction slots are implemented on the duct lower surface with the circumferential slot angels of 100° and 110° respectively. For all the throat Mach numbers, the engine face distortion coefficient is reduced to less than 1%, virtually eliminated by CFJ. Besides, the total pressure recovery is also significantly enhanced, especially at the high throat Mach number of 0.79. The study also indicates that a higher throat Mach number requires a lower CFJ power coefficient (P_C) to eliminate the flow separation and distortion. This numerical study suggests that it is possible to eliminate S-duct distortion by using CFJ active flow control.

8 Acknowledgment

The authors would like to acknowledge the computing resource provided by the Center for Computational Sciences at the University of Miami.

Disclosure: The University of Miami and Dr. Gecheng Zha may receive royalties for future commercialization of the intellectual property used in this study.

References

[1] K. A. Geiselhart, D. L. Daggett, R. Kawai, and D. Friedman, "Blended wing body systems studies: boundary layer ingestion inlets with active flow control." NASA Technical Report, NASA/CR-2003-212670, Langley Research Center; Hampton, VA, December 01, 2003.

[2] R. T. Kawai, D. M. Friedman, and L. Serrano, "Blended wing body (bwb) boundary layer ingestion (bli) inlet configuration and system studies." NASA Technical Report, NASA/CR-2006-214534, Langley Research Center; Hampton, VA, December 01, 2006.

[3] J. D. Mattingly, W. H. Heiser, and D. T. Pratt, *Aircraft engine design*. American Institute of Aeronautics and Astronautics, 2002.

[4] D. Miller and G. Addington, "Aerodynamic flowfield control technologies for highly integrated airframe propulsion flowpaths," in *2nd AIAA Flow Control Conference, AIAA 2004-2625, June, 20, 2004*.

[5] B. REICHERT and B. WENDT, "An experimental investigation of s-duct flow control using arrays oflow-profile vortex generators," in *31st Aerospace Sciences Meeting, AIAA 1993-0018, Reno,NV,11, 14 January*, 1993.

[6] B. H. Anderson and J. Gibb, "Study on vortex generator flow control for the management of inlet distortion," *Journal of Propulsion and Power*, vol. 9, no. 3, pp. 422–430, 1993.

[7] J. Gibb and M. Jackson, "Some preliminary results from tests using vortex generators in the circular/circular diffusing s-duct model m2129 test phase 3," *Defense research agency Rept. AP4 (92) WP15*, 1992.

[8] J. Gibb and B. Anderson, "Vortex flow control applied to aircraft intake ducts," in *Proceedings of the Royal Aeronautical Society Conf., High Lift and Separation Control, Paper*, no. 14, 1995.

[9] B. H. Anderson and J. Gibb, "Vortex-generator installation studies on steady-state and dynamic distortion," *Journal of aircraft*, vol. 35, no. 4, pp. 513–520, 1998.

[10] A. Jirasek, "Design of vortex generator flow control in inlets," *Journal of Aircraft*, vol. 43, no. 6, pp. 1886–1892, 2006.

[11] T. J. Burrows, Z. Gong, B. Vukasinovic, and A. Glezer, "Investigation of trapped vorticity concentrations effected by hybrid actuation in an offset diffuser," in *54th AIAA Aerospace Sciences Meeting, AIAA 2016-0055, San Diego, California,4-8 January*, 2016.

[12] T. J. Burrows, B. Vukasinovic, and A. Glezer, "Flow dynamics effected by active flow control in an offset diffuser," in *2018 Flow Control Conference, AIAA 2018-4024, June 25-29, 2018, Atlanta, Georgia.*

[13] N. A. Harrison, J. Anderson, J. L. Fleming, and W. F. Ng, "Active flow control of a boundary layer-ingesting serpentine inlet diffuser," *Journal of Aircraft*, vol. 50, no. 1, pp. 262–271, 2013.

[14] N. A. Harrison, *Active Flow Control of a Boundary Layer Ingesting Serpentine Diffuser*. Virginia Tech, 2005.

[15] I. Rudin, E. Arad, and J. Cohen, "Performance enhancement of boundary layer ingesting inlet using active flow control methods," in *2018 Applied Aerodynamics Conference,AIAA 2018-3066,Atlanta, Georgia, June 25-29*, 2018.

[16] G.-C. Zha, B. F Carroll, C. D. Paxton, C. A. Conley, and A. Wells, "High-performance airfoil using coflow jet flow control," *AIAA journal*, vol. 45, no. 8, pp. 2087–2090, 2007.

[17] A. Lefebvre, B. Dano, W. Bartow, M. Fronzo, and G. Zha, "Performance and energy expenditure of coflow jet airfoil with variation of mach number," *Journal of Aircraft*, vol. 53, no. 6, pp. 1757–1767, 2016.

[18] G. Zha, W. Gao, and C.D. Paxton, "Jet Effects on Co-Flow Jet Airfoil Performance," *AIAA Journal*, vol. 45, pp. 1222–1231, 2007.

[19] G.-C. Zha, C. Paxton, A. Conley, A. Wells, nd B. Carroll, "Effect of Injection Slot Size on High Performance Co-Flow Jet Airfoil," *AIAA Journal of Aircraft*, vol. 43, pp. 987–995, 2006.

[20] B. Wang, B. Haddoukessouni, J. Levy, and G.-C. Zha, "Numerical investigations of injection-slot-size effect on the performance of coflow jet airfoils," *Journal of Aircraft*, vol. 45, no. 6, pp. 2084–2091, 2008.

[21] B. P. E. Dano, D. Kirk, and G.-C. Zha, "Experimental Investigation of Jet Mixing Mechanism of Co- Flow Jet Airfoil." AIAA-2010-4421, 5th AIAA Flow Control Conference, Chicago, IL, 28 Jun - 1 Jul 2010.

[22] B. Dano, G. Zha, and M. Castillo, "Experimental study of co-flow jet airfoil performance enhancement using discreet jets." AIAA Paper 2011-941, 49th AIAA Aerospace Sciences Meeting including the New Horizons Forum and Aerospace Exposition, Orlando, Florida, 04 - 07 January 2011.

[23] Lefebvre, A. and Zha, G.-C. , "Design of High Wing Loading Compact Electric Airplane Utilizing Co-Flow Jet Flow Control." AIAA Paper 2015-0772, AIAA SciTech2015: 53nd Aerospace Sciences Meeting, Kissimmee, FL, 5-9 Jan 2015.

[24] Liu, Z.-X. and Zha, G.-C., "Transonic Airfoil Performance Enhancement Using Co-Flow Jet Active Flow Control." AIAA Paper 2016-3066, AIAA Aviation, Washington, D.C., June 13-17 2016.

[25] Lefebvre, A. and Zha, G.-C., "Trade Study of 3D Co-Flow Jet Wing for Cruise Performance." AIAA Paper 2016-0570, AIAA SCITECH2016, AIAA Aerospace Science Meeting, San Diego, CA, 4-8 January 2016.

[26] G. Zha, Y. Yang, Y. Ren, and B. McBreen, "Super-lift and thrusting airfoil of coflow jet actuated by micro-compressors," in *2018 Flow Control Conference, AIAA 2018-3061, Atlanta, Georgia, June 25-29*, 2018.

[27] J. Zhang, K. Xu, Y. Yang, Y. Ren, P. Patel, and G. Zha, "Aircraft control surfaces using co-flow jet active flow control airfoil." AIAA Paper 2018-3067, 2018 Applied Aerodynamics Conference, Atlanta, Georgia, June 25-29, 2018.

[28] K. Xu and G. Zha, "High control authority 3d aircraft control surfaces using co-flow jet." AIAA Journal of Aircraft (2020), accessed July 14, 2020.doi: 10.2514/1.C035727, 2020.

[29] K. Xu, J. Zhang, and G. Zha, "Drag minimization of co-flow jet control surfaces at cruise conditions." AIAA 2019-1848, AIAA Scitech 2019 Forum, San Diego, California, 7-11 January 2019.

[30] K. Xu, Y. Ren, and G. Zha, "Numerical investigation of nasa hump using co-flow jet for separation control." AIAA 2020-1058, 2020 AIAA SciTech Forum, Orlando, Florida, 6-10 January, 2020.

[31] K. Xu and G. Zha, "Mitigation of serpentine duct flow distortion using coflow jet active flow control," in *AIAA AVIATION 2020 FORUM,VIRTUAL EVENT, AIAA 2020-2954*, June 15-19, 2020.

[32] Y. Wang and G.-C. Zha, "Study of 3D Co-flow Jet Wing Induced Drag and Power Consumption at Cruise Conditions." AIAA Paper 2019-0034, AIAA SciTech 2019, San Diego, CA, January 7-11, 2019.

[33] Y. Wang and G.-C. Zha, "Study of Super-Lift Coefficient of Co-Flow Jet Airfoil and Its Power Consumption." Submitted to AIAA Aviation 2019, AIAA Applied Aerodynamics Conference, Dallas, Texas, 17-21 June 2019.

[34] P. Spalart and S. Allmaras, "A One-equation Turbulence Model for Aerodynamic Flows." AIAA-92-0439, 30th Aerospace Sciences Meeting and Exhibit, Reno, NV, U.S.A., 06 - 09 January 1992.

[35] Y.-Q. Shen, G.-C. Zha, and B.-Y. Wang, "Improvement of Stability and Accuracy of Implicit WENO Scheme ," *AIAA Journal*, vol. 47, pp. 331–344, 2009.

[36] Shen, Y.-Q. and Zha, G.-C. and Chen, X.-Y., " High Order Conservative Differencing for Viscous Terms and the Application to Vortex-Induced Vibration Flows," *Journal of Computational Physics*, vol. 228(2), pp. 8283–8300, 2009.

[37] Shen, Y.-Q. and Zha, G.-C. , " Improvement of the WENO Scheme Smoothness Estimator," *International Journal for Numerical Methods in Fluids*, vol. DOI:10.1002/fld.2186, 2009.

[38] G.-C. Zha, Y. Shen, and B. Wang, "An improved low diffusion E-CUSP upwind scheme ," *Journal of Computer & Fluids*, vol. 48, pp. 214–220, 2011.

[39] G.-C. Zha and E. Bilgen, "Numerical study of three-dimensional flows using unfactored upwind-relaxation sweeping algorithm," *Journal of Computational Physics*, vol. 125, no. 2, pp. 425–433, 1996.

[40] B. Wang, Z. Hu, and G.-C. Zha, "General subdomain boundary mapping procedure for structured grid implicit CFD parallel computation," *Journal of Aerospace Computing, Information, and Communication*, vol. 5, no. 11, pp. 425–447, 2008.

[41] B. Wang and G.-C. Zha, "Detached-eddy simulation of a coflow jet airfoil at high angle of attack," *Journal of aircraft*, vol. 48, no. 5, pp. 1495–1502, 2011.

[42] Y. Yang and G. Zha, "Super-lift coefficient of active flow control airfoil: What is the limit?." AIAA Paper 2017-1693, AIAA SCITECH2017, 55th AIAA Aerospace Science Meeting, Grapevine, January 9-13 2017.

[43] Im, H.-S. and Zha, G.-C. and Dano, B. P. E., "Large Eddy Simulation of Coflow Jet Airfoil at High Angle of Attack," *Journal of Fluid Engineering, vol. 136(2), p. 021101*, 2014.

[44] J. Dudek, "S-duct inlet with and without vortex generator validation cases." NPARC Alliance Verification and Validation Archive, https://www.grc.nasa.gov/WWW/wind/valid/sduct/sduct.html, 02 Mar 2009.

[45] Advisory Group for Aerospace Research and Development (AGARD), "Air intakes for high speed vehicles." Fluid Dynamics Panel Working Group 13, AR-270, Fort Worth, TX, Sep 1991.

[46] J. Seddon and E. Goldsmith, *Intake Aerodynamics*. AIAA Inc., New York, 1985.

[47] A. Willmer, T. Brown, and E. Goldsmith, "Effects of intake geometry on circular pitot intake performance at zero and low forward speeds." Aerodynamics of Power Plant Installation, AGARD CP301, Paper 5, Toulouse, France, May, 1981.

[48] J. C. Dudek, "Modeling vortex generators in a navier-stokes code," *AIAA journal*, vol. 49, no. 4, pp. 748–759, 2011.

[49] K. Xu and G. Zha, "Investigation of coflow jet active flow control for wind turbine airfoil." AIAA Paper 2020-2942, AIAA AVIATION Forum and Exposition, virtual event, 15-19 June, 2020.

[50] B. Anderson and J. Gibb, "Vane effector installation studies on steady state and dynamic inlet distortion," vol. AIAA Paper 1996-3279, 1996.